Voronoi-cell finite difference method for accurate electronic structure calculation of polyatomic molecules on unstructured grids

Sang-Kil Son[a,1]

[a]*Department of Chemistry, University of Kansas, Lawrence, KS 66045, USA*

Abstract

We introduce a new numerical grid-based method on unstructured grids in the three-dimensional real-space to investigate the electronic structure of polyatomic molecules. The Voronoi-cell finite difference (VFD) method realizes a discrete Laplacian operator based on Voronoi cells and their natural neighbors, featuring high adaptivity and simplicity. To resolve multicenter Coulomb singularity in all-electron calculations of polyatomic molecules, this method utilizes highly adaptive molecular grids which consist of spherical atomic grids. It provides accurate and efficient solutions for the Schrödinger equation and the Poisson equation with the all-electron Coulomb potentials regardless of the coordinate system and the molecular symmetry. For numerical examples, we assess accuracy of the VFD method for electronic structures of one-electron polyatomic systems, and apply the method to the density-functional theory for many-electron polyatomic molecules.

Keywords: Voronoi-cell finite difference, VFD, Schrödinger equation, numerical grid-based method, density-functional theory, DFT, polyatomic molecules, unstructured grids
PACS: 31.15.xf, 31.15.A-, 31.13.E-, 02.70.Bf

1. Introduction

The structure and motion of electrons in molecules are the most fundamental topics in atomic and molecular physics. To capture a picture of and ultimately gain a control of the electronic motions within molecules in attosecond science [1] demands accurate and efficient numerical simulations for the electronic structure and dynamics in molecules. For the electronic structure of the ground and low-lying excited states, the most conventional methods is the basis set expansion method based on linear combination of atomic orbitals (LCAO) [2]. Despite its great achievement in quantum chemistry, it may not be adequate to explore electronic dynamics covering long-range motions of the electrons, because its computational space is usually confined to the localized atomic orbitals. On the other side, numerical grid-based methods to solve the Hamiltonian directly represented in real-space grids [3] have been employed for describing electronic dynamics in atomic and molecular physics. The computational space can be enlarged by including long-range grid points to simulate the excited and continuum states in electronic dynamics. Nonetheless, the grid-based method may need local refinement of grid points for accurate electronic structure calculations due to the characteristics of the Coulomb potential, which is one of complications in the widely used uniform grid methods [4].

The Coulomb potential ($=1/r$) in the all-electron Hamiltonian of atoms and molecules incorporates cusps at nuclear positions in electronic wavefunctions, which is called Coulomb singularity [5] that significantly affects accuracy of electronic bound states. The realistic Coulomb potential also influences highly excited and continuum electrons due to its long-range behavior. To obtain both the short- and long-range manners of the realistic Coulomb potential, Chu and colleagues [6, 7, 8, 9, 10] have developed generalized pseudospectral (GPS) method on a nonuniform grid system which has denser grid points near the nuclear positions and sparser grid points away from the nuclei. For atomic systems with the spherical coordinates [7] and diatomic systems with the prolate spheroidal coordinates [8, 9, 10], the GPS method has achieved machine accuracy for electronic structures and a remarkable success in calculations of strong-field electronic dynamics such as multiphoton ionization and high-order harmonic generation (for examples, see Ref. [6] and references therein).

As the number of nuclei goes beyond uniatomic and diatomic systems, however, it is not trivial to employ a coordinate system suitable for arbitrary geometries of polyatomic molecules. From this viewpoint, numerical methods on unstructured grids [11], which have no fixed connectivity between grid points, become much attractive for calculations of polyatomic molecules, because the unstructured grid scheme enables us to use highly adaptive nonuniform molecular grids with variable resolutions around nuclear positions, regardless of the coordinate system and the molecular symmetry.

For a molecular grid system, it is natural to consider that molecular grids consist of spherical atomic grids centered at nuclear positions, which can be called multicenter molecular grids. This intuitive idea was introduced and implemented by

Email address: sangkil.son@cfel.de (Sang-Kil Son)
[1]Present address: Center for Free-Electron Laser Science, DESY, 22607 Hamburg, Germany

Becke [12] and Becke and Dickson [13] for basis-set-free DFT calculations. Becke's procedure was based on multicenter numerical integration [14] and solved the Schrödinger equation by means of the single-center decomposition with spherically-averaged approximation [15], rather than a direct solution on molecular grids. A direct solution on such a multicenter molecular grid distribution is most desirable but not trivial with conventional numerical grid-based methods.

To directly solve the Schrödinger equation or more generally the partial differential equations (PDE) on unstructured grids (e.g. multicenter molecular grids), one can imagine the Voronoi diagram [16], enclosing each grid point in each cell. Because the Voronoi diagram is geometrically attractive and versatile, there have been tremendous applications in various areas of science and engineering over one century [17, 18]. However, a PDE solver exploiting geometrical advantages of the Voronoi diagram has not been considered until relatively recent years. In geophysics and solid mechanics, the natural element method (NEM) [19] and the natural neighbor Galerkin method (NNGM) [20, 21] have been developed to realize PDE solutions on unstructured grids with the help of the Voronoi diagram. The concept of the Voronoi diagram has been employed within the finite volume method [22, 23] and the particle-in-cell method [24]. Recently, Sukumar [25] and Sukumar and Bolander [26] proposed the discrete Laplacian operator on unstructured grids based on the finite difference scheme with Voronoi cells and natural neighbors, and named it the Voronoi-cell finite difference (VFD) method. Because there is no restriction on the location of grid points, the VFD method with arbitrary unstructured grids is regarded as a meshfree (or meshless) method which is of current interest in computer modeling and simulation in engineering applications [27, 28]. Even though an idea to exploit the Voronoi diagram in the electronic structure calculation has been reported [29], no practical implementation in this direction has been accomplished until recently.

In this paper, we extend VFD to solve the Schrödinger, Kohn–Sham, and Poisson equations for accurate electronic structures of polyatomic molecules with the all-electron realistic Coulomb potential on multicenter molecular grids in the three-dimensional (3D) real-space. There have been many grid-based approaches suggested to attack the multicenter Coulomb singularity with local grid refinement in real-space: for examples, finite element [30, 31, 32, 33], spectral element [34], curvilinear adaptive coordinate [35, 36], multigrid [37, 38, 39], multiresolution analysis with wavelet [40, 41, 42], multicenter B-spline [43], and a hybrid combination of basis set expansion and discrete variable representation [44] (for more examples, see Ref. [3] and references therein). In addition, one of the most popular grid-based methods has been the high-order finite difference method with the pseudopotential on uniform Cartesian grids [45, 46], and alternatively the plane-wave method combined with the pseudopotential also has been widely used for periodic systems [47]. Notable features of the proposed VFD method over these previous approaches are summarized as follows: (i) High adaptivity: by means of unstructured grids there is no restriction on local grid refinement for polyatomic molecules regardless of molecular symmetry. (ii) Simplicity: VFD provides a simple and explicit matrix form of the discrete Laplacian operator, which realizes a direct solution of the Schrödinger equation on unstructured grids, as well as a simple implementation of the Poisson equation. (iii) No massive integration: the potential matrix is given by a value at each grid point and the Hamiltonian matrix is constructed without any integration. (iv) Realistic Coulomb potential: VFD allows us to use the realistic Coulomb potential in 3D rather than model potentials, so that we correctly simulate the short- and long-range features of the Coulomb potential.

This paper is organized as follows. In Sec. 2, we introduce the Voronoi-cell finite difference method including the Voronoi discretization, discrete Laplacian operator, symmetric Hamiltonian matrix, and nodal integration scheme. We also propose a multicenter molecular grid system suitable for arbitrary shapes of polyatomic molecules. Section 3 contains numerical results performed by the VFD method. Electronic structures of linear H_2^+ and triangular H_3^{++} are computed for accuracy tests of the Schrödinger equation with the realistic Coulomb potential. Accuracy of VFD nodal integration is also discussed. We present numerical grid-based DFT calculations for nitrogen, water, and benzene molecules. Eigenvalues and total energies are compared with uniform grid calculations and LCAO calculations with huge basis sets. It is followed by conclusion in Sec. 4.

2. Theory and computational details

2.1. Voronoi discretization

Let us consider an arbitrarily distributed grid-point set $\{\mathbf{x}_i\}$ in n-dimensions. A Voronoi cell surrounding a grid point of $\mathbf{x}_i$ is defined by a set of points that are closer to $\mathbf{x}_i$ than to any other grid points [18],

$$T_i = \{\mathbf{x} \in \mathbb{R}^n : d(\mathbf{x}, \mathbf{x}_i) \leq d(\mathbf{x}, \mathbf{x}_j) \text{ for } \forall\, j \neq i\}, \tag{1}$$

where $d(\mathbf{x}, \mathbf{y}) = \|\mathbf{x} - \mathbf{y}\|$ is an Euclidean distance between two points $\mathbf{x}$ and $\mathbf{y}$. It is well known that the Voronoi diagram is uniquely defined for a given grid-point set [18]. Figure 1 shows one example of a Voronoi diagram in 2D and some related symbols that are defined as follows. From the Voronoi diagram, the whole space is uniquely discretized into Voronoi cells, and each Voronoi cell is enclosed by surfaces between two adjacent Voronoi cells.

The Voronoi cell is denoted as T_i enclosing the ith grid point, and its volume is given by v_i. A Voronoi facet s_{ij} is the surface where two adjacent T_i and T_j meet together. Note that the Voronoi facet is a line in 2D (also called the Voronoi edge) as shown in Fig. 1 and a polygon plane in 3D. h_{ij} is a distance between the ith and jth grid points,

$$h_{ij} = \|\mathbf{x}_j - \mathbf{x}_i\|. \tag{2}$$

One of the Voronoi properties is that s_{ij} is the perpendicular bisector of h_{ij}. A natural neighbor [48] is defined by the fact that if two grid points share a common Voronoi facet, they are natural neighbors. A Voronoi vertex is defined as the point where Voronoi facets converge. In other words, the Voronoi facet between two neighboring grid points is surrounded by the Voronoi

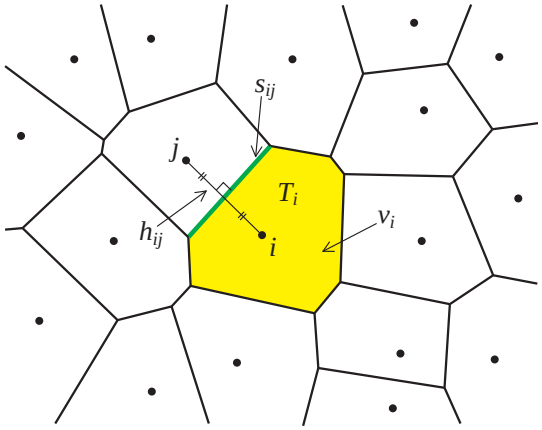

Figure 1: Voronoi diagram.

vertices belonging to the two grid points. Therefore, an area of s_{ij} in 3D (or a length in 2D) can be computed using the position of the surrounding vertices. In the 3D case, the area of the polygon is computed by the summation of the signed areas of triangles,

$$s_{ij} = \frac{1}{2}\left|\sum_{k=1}^{M} A(\mathbf{p}_k, \mathbf{p}_{k+1}, \mathbf{q})\right|, \tag{3}$$

where $\mathbf{q} = (\mathbf{x}_i + \mathbf{x}_j)/2$, $\{\mathbf{p}_k\}$ ($k = 1, \ldots, M$ with $\mathbf{p}_1 = \mathbf{p}_{M+1}$) are position vectors of the vertices, and M is the number of surrounding vertices for s_{ij}. The signed area A is given by $|A(\mathbf{p}_k, \mathbf{p}_{k+1}, \mathbf{q})| = \|(\mathbf{p}_k - \mathbf{q}) \times (\mathbf{p}_{k+1} - \mathbf{q})\|$, and the sign of A is positive when $\mathbf{p}_k$, $\mathbf{p}_{k+1}$, and $\mathbf{q}$ are oriented counterclockwise and negative when clockwise. The Voronoi cell T_i is further decomposed into polygonal pyramids that have their apex at the ith grid point and their base as each Voronoi facet. Thus v_i can be computed by the sum of volumes of these polygonal pyramids,

$$v_i = \frac{1}{6}\sum_{j}^{\text{neighbors}} h_{ij} s_{ij}, \tag{4}$$

where j runs over natural neighboring grid points of the ith grid point.

Therefore, for a given set of arbitrarily distributed grid points, v_i, s_{ij}, and h_{ij} are easily calculated in the Voronoi diagram. For numerical determination of the Voronoi diagram in 3D, we employ the Qhull package [49].

2.2. Voronoi-cell finite difference

The discrete Laplacian operator in the VFD scheme was proposed by Sukumar and colleagues [25, 26], and its symmetric form has been applied to solve the time-dependent Schrödinger equation [50, 51]. Here we focus on the explicit expressions of the Hamiltonian matrix elements to solve the time-independent Schrödinger equation in detail.

From the Gauss' theorem [52], the Laplacian of φ is written as,

$$\boldsymbol{\nabla}^2\varphi = \lim_{\int_V d\tau \to 0} \frac{\int_S \boldsymbol{\nabla}\varphi \cdot \mathbf{n}\, d\sigma}{\int_V d\tau}, \tag{5}$$

which is exact in the limit of a vanishing volume. Here $\mathbf{n}$ is the normal unit vector of the surface S. To find the discrete Laplacian form at a grid point i, imagine the Voronoi cell corresponding to the ith grid point. After the Voronoi discretization, the volume integral is given by the Voronoi volume v_i,

$$\int_{V \subset T_i} d\tau \to v_i, \tag{6}$$

and the surface integral is decomposed into the areas of the Voronoi facets s_{ij},

$$\int_{S \subset \partial T_i} \boldsymbol{\nabla}\varphi \cdot \mathbf{n}\, d\sigma \to \sum_{j}^{\text{neighbors}} (\boldsymbol{\nabla}\varphi)_i \cdot \mathbf{n}_{ij} s_{ij}, \tag{7}$$

where ∂T_i indicates the boundary surface of T_i and $\mathbf{n}_{ij}$ is the normal vector of the corresponding Voronoi facet s_{ij}. The inner product indicates a directional derivative of φ, which is given by the projection of $\boldsymbol{\nabla}\varphi$ on the normal vector of the Voronoi facet. Because a line between neighboring grid points i and j is perpendicular to the corresponding Voronoi facet, the directional derivative at the ith grid point in the direction to neighboring grid point j can be evaluated by the simple difference scheme,

$$(\boldsymbol{\nabla}\varphi)_i \cdot \mathbf{n}_{ij} \approx \frac{\varphi_j - \varphi_i}{h_{ij}}. \tag{8}$$

Thus the discrete Laplacian at the ith grid point of the Voronoi-cell finite difference can be evaluated as

$$\left(\boldsymbol{\nabla}^2\varphi\right)_i = \frac{1}{v_i}\sum_{j}^{\text{neighbors}} \frac{\varphi_j - \varphi_i}{h_{ij}} s_{ij}. \tag{9}$$

Note that this scheme relies on two computational approximations: firstly the volume of Voronoi cell is small in Eq. (5), and secondly a finite difference scheme is used for the directional derivative in Eq. (8).

Using the Voronoi-cell finite difference scheme, let us consider the Schrödinger equation for one electron in 3D,

$$\left[-\frac{1}{2}\boldsymbol{\nabla}^2 + U(\mathbf{x})\right]\psi(\mathbf{x}) = \varepsilon\psi(\mathbf{x}), \tag{10}$$

where $\psi(\mathbf{x})$ is a wavefunction (eigenfunction) and ε is an energy (eigenvalue). The boundary condition of the wavefunction is zero at a large distance, i.e., $\psi(\mathbf{x}) = 0$ as $|\mathbf{x}| \to \infty$. Note that the atomic units are used throughout the paper.

The matrix form of this eigenvalue problem to be solved is

$$\mathbf{HC} = \mathbf{CE}, \tag{11}$$

where $\mathbf{C}$ is the eigenvector matrix, $\mathbf{E}$ is the diagonal matrix of eigenvalues, and $\mathbf{H}$ is the Hamiltonian matrix which is given by $\mathbf{H} = -\mathbf{L}/2 + \mathbf{U}$. From the discrete Laplacian in Eq. (9), $\mathbf{L}$ is expressed as

$$L_{ij} = \begin{cases} -\dfrac{1}{v_i}\displaystyle\sum_{k}^{\text{neighbors}} \frac{s_{ik}}{h_{ik}} & (i = j), \\ \dfrac{1}{v_i}\dfrac{s_{ij}}{h_{ij}} & (i,\ j\text{: neighbors}), \\ 0 & (\text{otherwise}), \end{cases} \tag{12}$$

and $\mathbf{U}$ is diagonal and simply given by a potential value at each grid point without any integration,

$$U_{ij} = \delta_{ij} U(\mathbf{x}_i). \tag{13}$$

Using the symmetrization technique introduced in Ref. [51], one obtains the symmetric form of Eq. (11),

$$\tilde{\mathbf{H}}\tilde{\mathbf{C}} = \tilde{\mathbf{C}}\mathbf{E}, \tag{14}$$

where $\tilde{\mathbf{C}} = \mathbf{V}^{\frac{1}{2}}\mathbf{C}$ and $\tilde{\mathbf{H}} = -\tilde{\mathbf{L}}/2 + \mathbf{U} = -\mathbf{V}^{\frac{1}{2}}\mathbf{L}\mathbf{V}^{-\frac{1}{2}}/2 + \mathbf{U}$. Here $\mathbf{V}$ is a diagonal matrix of Voronoi volumes, $V_{ij} = \delta_{ij} v_i$. Since it is diagonal, evaluations of $\mathbf{V}^{\frac{1}{2}}$ and $\mathbf{V}^{-\frac{1}{2}}$ are trivial. Now $\tilde{\mathbf{L}}$ is symmetric and its off-diagonal matrix elements are given by $\tilde{L}_{ij} = L_{ij}\sqrt{v_i/v_j} = s_{ij}/h_{ij}\sqrt{v_i v_j}$ (i, j: neighbors).

After $\tilde{\mathbf{H}}$ is solved, the eigenvectors are recovered by $\mathbf{C} = \mathbf{V}^{-\frac{1}{2}}\tilde{\mathbf{C}}$,

$$c_i^{(k)} = \frac{\tilde{c}_i^{(k)}}{\sqrt{v_i}}, \tag{15}$$

where $c_i^{(k)}$ and $\tilde{c}_i^{(k)}$ are values at the ith grid point of the kth eigenvector of $\mathbf{H}$ and $\tilde{\mathbf{H}}$, respectively. Note that for electronic structure calculations of polyatomic molecules, $c_i^{(k)}$ has cusps in the vicinity of nuclear positions due to the Coulomb singularity. If grid distribution is designed to let v_i be small enough around nuclear positions, the solution of $\tilde{c}_i^{(k)}$ can be smoothed out near cusps of $c_i^{(k)}$ because of Eq. (15). A multicenter molecular grid distribution is introduced in Sec. 2.5 for this purpose.

Also $\{v_i\}$ work as weight functions when integration is required. Since the whole space is discretized by the Voronoi cells, the integration over the space is approximated by the nodal quadrature method [53] without additional background cells or grid points,

$$\int_V f(\mathbf{x}) d\tau \approx \sum_i f(\mathbf{x}_i) v_i. \tag{16}$$

The numerical error of this nodal quadrature is analyzed in Sec. 3.2.

2.3. Comparison with other methods

A remarkable distinction between VFD and ordinary finite difference (FD) method with regular uniform grids is that VFD on unstructured grids can accommodate any types of grid distributions. Thus the VFD method is compared with the generalized finite difference (GFD) method [54, 55] that also can accommodate irregular grids. GFD usually employs the Taylor expansion and solves a linear system of equations to compute the first and second derivative quantities at every grid point. Therefore GFD does not provide explicit expressions of the Laplacian matrix elements and in many cases the matrix involved in the linear system of equations becomes ill-conditioned, whereas VFD offers the explicit forms of the Laplacian matrix elements that unconditionally exist.

The VFD method is comparable with the finite element (FE) method because of high adaptivity of grid distributions. The difference is that VFD expressions are given only at each grid, while FE performs calculations by use of interpolations. In fact, VFD can be equivalently derived from the second-order non-Sibsonian interpolation based on Voronoi diagram in the FE framework [20]. Note that advantage of VFD over FE is its simple and explicit expressions.

Also the VFD method is compared with the finite volume (FV) method [56, 57, 58] because both are based on the Gauss' theorem and utilize cell volumes for the basic formulae. However, VFD differs from FV in the integration method as the following. VFD simply replaces the volume integral with the Voronoi volume and the surface integral with the summation of the directional derivatives over natural neighbors, while FV generally evaluates those integrals using the quadrature method with additional background grid points.

2.4. Application to density-functional theory

The density-functional theory (DFT) states the total energy can be obtained by energy functional [59],

$$E_{\text{total}} = E[\rho] = T_{\text{s}}[\rho] + J[\rho] + E_{\text{ne}}[\rho] + E_{\text{xc}}[\rho], \tag{17}$$

where ρ is the total density. $T_{\text{s}}[\rho]$ is the noninteracting kinetic energy functional, $J[\rho]$ the classical electron–electron repulsion energy functional, and $E_{\text{ne}}[\rho]$ the nucleus–electron Coulomb interaction energy functional. For simplicity, the exchange–correlation functional $E_{\text{xc}}[\rho]$ used in this paper is the local density approximation (LDA) [60], combined with the Vosko–Wilk–Nusair (VWN) correlation functional [61] whose practical implementation is found in Ref. [62].

In the Kohn–Sham DFT formulation [63], one solves the Schrödinger-like equation,

$$\left[-\frac{1}{2}\boldsymbol{\nabla}^2 + u_{\text{eff}}(\mathbf{x})\right]\psi_i(\mathbf{x}) = \varepsilon_i \psi_i(\mathbf{x}), \tag{18}$$

where the effective potential $u_{\text{eff}}(\mathbf{x})$ is expressed by

$$u_{\text{eff}}(\mathbf{x}) = u_{\text{ne}}(\mathbf{x}) + u_{\text{h}}(\mathbf{x}) + u_{\text{xc}}(\mathbf{x}). \tag{19}$$

Here, $u_{\text{ne}}(\mathbf{x})$ is given by nucleus–electron Coulomb interaction and $u_{\text{xc}}(\mathbf{x})$ used is the LDA potential. Both are simply given by a value at each grid point. The Hartree potential $u_{\text{h}}(\mathbf{x})$ is computed by solving the Poisson equation,

$$\boldsymbol{\nabla}^2 u_{\text{h}}(\mathbf{x}) = -4\pi\rho(\mathbf{x}). \tag{20}$$

Its discrete form $\mathbf{u}_{\text{h}}$ is simply solvable by a linear system solution of the Laplacian matrix in VFD,

$$\mathbf{L}\mathbf{u}_{\text{h}} = -4\pi\boldsymbol{\rho}, \tag{21}$$

where $\mathbf{u}_{\text{h}}$ and $\boldsymbol{\rho}$ are vector forms of the Hartree potential and the total density, respectively, represented in grid points. $\mathbf{L}$ is the sparse Laplacian matrix in VFD derived from Eq. (9).

The boundary condition for the Hartree potential is asymptotically given by Q/r where Q is the total charge of electrons, when a radius r is large enough. In present calculations, the maximum r is about 150 a.u. This boundary condition is easily implemented as follows. The known conditions are put into the

outermost grid points and employed to solve unknown $\mathbf{u}_\mathrm{h}$ values. Let w_i be the ith element of the $\mathbf{u}_\mathrm{h}$ vector. The ith row in Eq. (21) is expressed as $\sum_j L_{ij} w_j = -4\pi\rho_i$ where j runs over all grid points. Then the unknown potential values $\{w_{j'}\}$ are determined by

$$\sum_{j'} L_{ij'} w_{j'} = -4\pi\rho_i - \sum_{k}^{\text{boundary}} L_{ik} w_k, \tag{22}$$

where j' runs over grid points inside the boundary, k runs over the boundary grid points, and $w_k = Q/r_k$. For the symmetric Laplacian matrix $\tilde{\mathbf{L}}$, one can obtain the following expression after the transformation,

$$\sum_{j'} \tilde{L}_{ij'} w_{j'} \sqrt{v_{j'}} = -4\pi\rho_i \sqrt{v_i} - \sum_{k}^{\text{boundary}} \tilde{L}_{ik} w_k \sqrt{v_k}. \tag{23}$$

Note that the Poisson equation is solved with the same local grid refinement as the Schrödinger equation or the Kohn–Sham equation.

2.5. Multicenter molecular grids

In the real-space grid method, local refinement around nuclear positions is required to capture the Coulomb singularity. It is natural and intuitive to consider spherical atomic grids located at nuclear positions and combine them together to have more grid points near the nuclei. Figure 2 shows 2D sketches of three different types of multicenter molecular grids in this manner of composite grids. Note that all calculations are done in 3D molecular grid systems. (a) Non-overlapping composite grids: the atomic grids are combined and the grid points in the overlapping region are removed except ones closer to the atom that each grid point belongs to. As a result, the sphere of the atomic grids is cut out when it overlaps with others. (b) Overlapping composite grids: all overlapping grid points are kept except two grid positions exactly coincide. (c) Squeezed composite grids: to avoid the overlap, the maximum radius of the atomic grids is varied when it meets with others. As a result, the sphere of the atomic grids is squeezed. Among these three types, the non-overlap one has the smallest number of grid points because some grid points in the overlap are cut out.

To achieve more local refinement in the vicinity of nuclear positions, the radial part of the spherical atomic grids is generated by an algebraic mapping function [64],

$$r(x) = L\frac{1+x}{1-x} \quad (-1 < x < 1), \tag{24}$$

where L is a mapping parameter and x is defined as uniform grid points in 1D,

$$x_i = \frac{2i}{N_r+1} - 1 \quad (i = 1, \cdots, N_r), \tag{25}$$

where N_r is the number of radial grids. Thus, the grid location in the radius ranges from $L/(2N_r+1)$ to LN_r, realizing dense grid points near the nuclear position, but not coinciding with the nuclear position.

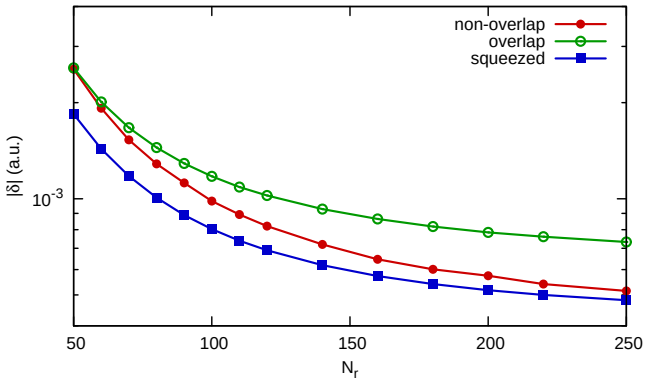

Figure 3: Comparison of numerical accuracy for different types of multicenter molecular grids.

For the angular part, the Lebedev quadrature [65] is widely used for multicenter numerical integration [14]. The angular grid distribution of the Lebedev quadrature is adopted here for the spherical atomic grids. For a given l_max, the number of angular grids is estimated by $N_\mathrm{ang} \approx 4(l_\mathrm{max}+1)^2/3$.

Therefore, there are only three parameters to construct atomic grids: N_r and L for the radial part, and l_max for the angular part of individual atomic grids. Then the atomic grids are placed at each nuclear position of a molecule and multicenter molecular grids are constructed according to different types in Fig. 2. Note that the grid distribution of the overlapping composite grids in this manner is exactly matched to the one used in Becke's basis-set-free DFT calculation [12, 13]. Differences from Becke's scheme are that in VFD there is no single-center decomposition and the Schrödinger equation is directly solvable on this grid distribution, which remarkably simplifies the numerical algorithm and implementation.

3. Results and Discussion

3.1. Electronic structure of one-electron systems

First, three different types of multicenter molecular grids proposed in Sec. 2.5 are tested. Figure 3 compares numerical accuracy for choosing three different types as a function of N_r. The y-axis represents absolute errors $|\delta|$ on the ground-state energy of H_2^+, defined by differences between computed values with VFD and an exact value [66]. N_r is varied, and L=1 and l_max=20 are fixed. As N_r increases, the ground energies are converged to the exact value. Unresolved errors at large N_r are due to small l_max, which can be reduced as l_max increases. The squeezed type always shows better convergence and the overlap type does worse than others, while the non-overlap type becomes close to the squeezed type when N_r increases. The reason of inferior convergence of the overlap type is not clear and it may need further analysis. Because the non-overlap type has the smallest total number of grid points at given N_r and l_max, we will use the non-overlap type for further calculations.

Next, we perform accuracy tests for H_2^+ with respect to N_r and l_max. Figures 4(a) and 4(b) plot absolute errors $|\delta|$ on the

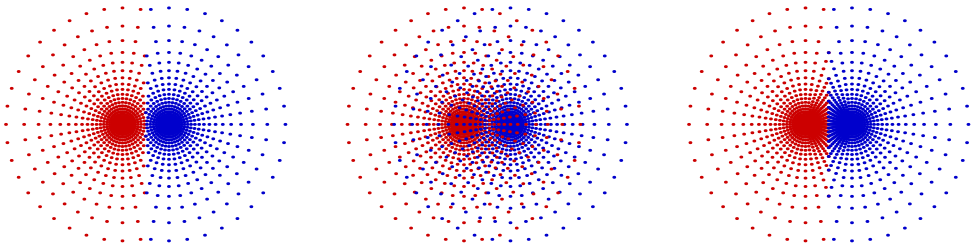

(a) Non-overlap (b) Overlap (c) Squeezed

Figure 2: 2D sketches of different types of multicenter molecular grids

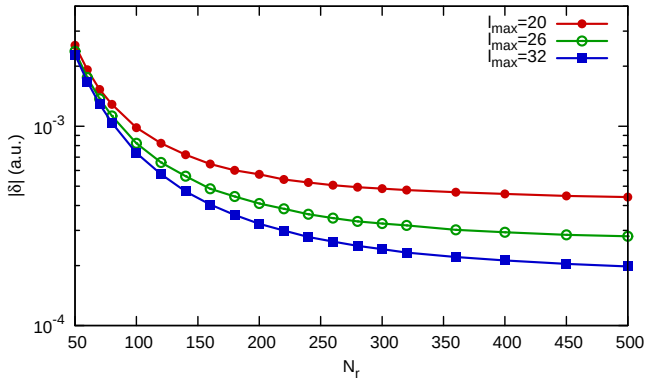

(a) Convergence as N_r increases.

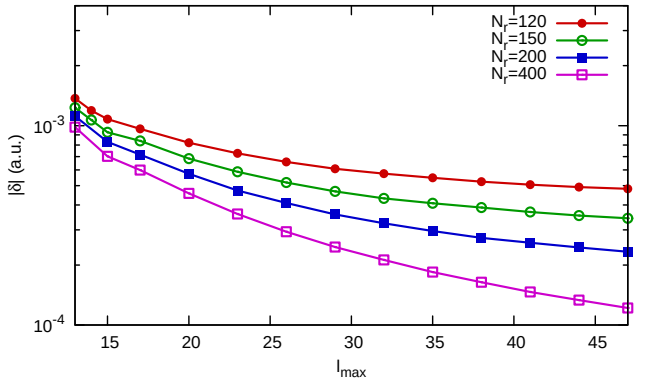

(b) Convergence as $l_{\max}$ increases.

Figure 4: Accuracy on the ground-state energies of H_2^+ computed by VFD.

ground-state energy of H_2^+ as a function of N_r and $l_{\max}$, respectively. The internuclear distance is fixed at R=2.0 a.u. Errors are getting smaller as N_r and $l_{\max}$ increase, confirming that accuracy of the VFD method is systematically improved by increasing the number of grid points to compute electronic structures with the realistic Coulomb potential. Note that low-lying excited states show similar trends of convergence as the ground state. Figure 4 indicates that the ground-state energies are converged up to the third decimal place, i.e., $|\delta| < 1\times10^{-3}$ a.u. with $N_r \geq 100$ and $l_{\max} \geq 20$, or $N_r \geq 120$ and $l_{\max} \geq 17$.

Table 1 lists electronic energies of low-lying bound states of H_2^+ up to first 16 states. All computed energies are lower by less than 2.57×10^{-4} a.u. from the exact values [66] and all error percentages are less than 0.12%. N_r=400, L=1 and $l_{\max}$=47 are used with the non-overlap type of molecular grids. The matrix dimension with these parameters is approximately 2 millions (N_{grid}=2,086,662) but it becomes very sparse because VFD considers only closest natural neighbors of each grid point. Eigenvalues of this huge real symmetric sparse matrix are determined by the implicitly restarted Lanczos method of ARPACK [67] and the large sparse matrix solver of PARDISO [68]. The computation time to solve selected eigenvalues of the 2,086,662×2,086,662 matrix takes about 1.2 h on the lab workstation equipped with two Intel Xeon X5355 (quad core, 2.66 GHz) CPUs. For comparison, Table 1 includes results from LCAO performed by GAMESS [69] with a huge basis set of aug-cc-pV6Z [70] that converges systematically to the complete basis set limit. For the ground and first excited states, the LCAO results agree well with exact values but there are remarkable discrepancies in higher excited states. This is not surprising because atomic-centered basis functions in LCAO are optimized for the ground state calculation. On the other hand, VFD results show fair agreements for all ground and excited states.

Next, we compute the simplest one-electron triatomic molecule, H_3^{++}, that has the equilateral triangular shape. It has been known that triangular H_3^{++} does not exist [71] but there have been a few results for the ground state with a fixed internuclear distance computed by LCAO and the finite element (FE) method [30] as the accuracy assessment beyond atoms and diatomic molecules. We note that there have been recent

Table 1: Electronic energies (in a.u.) and absolute errors $|\delta|$ of the ground and excited states of H_2^+ at R=2.0 a.u. The number in parentheses in orbital symmetry indicates degeneracy and the number in brackets indicates the power of 10.

Orbital	Exact[a]	LCAO[b]		VFD[c]	
		$\|\delta\|$ (a.u.)	$\|\delta\|$ (%)	$\|\delta\|$ (a.u.)	$\|\delta\|$ (%)
$1\sigma_g$	−1.102 634	1.41[−6]	0.00	1.22[−4]	0.01
$1\sigma_u$	−0.667 534	1.69[−6]	0.00	1.55[−4]	0.02
$1\pi_u(2)$	−0.428 772	1.09[−4]	0.03	7.92[−5]	0.02
$2\sigma_g$	−0.360 865	5.29[−5]	0.01	6.65[−5]	0.02
$2\sigma_u$	−0.255 413	2.49[−4]	0.10	7.14[−5]	0.03
$3\sigma_g$	−0.235 778	3.46[−3]	1.47	1.20[−4]	0.05
$1\pi_g(2)$	−0.226 700	4.23[−3]	1.87	1.81[−4]	0.08
$1\delta_g(2)$	−0.212 733	5.40[−2]	25.40	2.57[−4]	0.12
$2\pi_u(2)$	−0.200 865	6.02[−2]	29.97	7.81[−5]	0.04
$4\sigma_g$	−0.177 681	1.39[−3]	0.78	7.70[−5]	0.04
$3\sigma_u$	−0.137 313	6.44[−3]	4.69	8.55[−5]	0.06
$5\sigma_g$	−0.130 792	3.77[−2]	28.82	1.05[−4]	0.08

[a]Reference [66]
[b]Basis set: aug-cc-pV6Z
[c]Grid parameters: N_r=400, L=1, and $l_{\max}$=47

Table 2: Electronic energies (in a.u.) of the ground and excited states of equilateral triangular H_3^{++} at R=1.68 a.u. $\Delta=E_{\rm VFD}-E_{\rm LCAO}$ and the number in brackets indicates the power of 10.

Orbital	FE[a]	LCAO[b]	VFD[c]	Δ
$1a_1'$	−1.909 571	−1.909 569	−1.909 787	−2.18[−4]
$1e'(2)$		−1.138 578	−1.138 979	−4.02[−4]
$1a_2''$		−0.869 699	−0.870 008	−3.10[−4]
$2a_1'$		−0.704 969	−0.705 131	−1.62[−4]
$2e'(2)$		−0.534 978	−0.535 372	−3.93[−4]
$3e'(2)$		−0.484 387	−0.485 081	−6.94[−4]
$1e''(2)$		−0.481 488	−0.481 732	−2.44[−4]
$3a_1'$		−0.479 498	−0.480 741	−1.24[−3]
$2a_2''$		−0.415 434	−0.422 375	−6.94[−3]
$4a_1'$		−0.362 325	−0.362 826	−5.01[−4]
$4e'(2)$		−0.283 203	−0.295 392	−1.22[−2]

[a]Reference [30]
[b]Basis set: aug-cc-pV6Z
[c]Grid parameters: N_r=400, L=1, and $l_{\max}$=41

discussions on existence of triangular H_3^{++} in strong magnetic fields [71]. Table 2 lists the ground- and excited-state electronic energies of H_3^{++} from VFD. For comparison, it includes the results from FE [30] and from LCAO with the aug-cc-pV6Z basis set. The distance between nuclei is fixed at R=1.68 a.u. For grid parameters, N_r=400, L=1, and $l_{\max}$=41 are used. Note that all VFD results in Table 2 are converged up to the third decimal place with respect to the number of grid points. Differences between VFD and LCAO ($\Delta=E_{\rm VFD}-E_{\rm LCAO}$) get increased for higher excited states.

3.2. Tests of nodal integration

Since energy functionals for DFT calculations in Eq. (17) involve integrals over the whole space, accuracy of VFD nodal quadrature integration of Eq. (16) must be preliminarily assessed for DFT energy calculations. Table 3 shows VFD integrals computed by Eq. (16) using converged density from LCAO calculations and corresponding exact values of integrals. Error percentages δ(%) of VFD integrals from exact values are also included. Molecular systems are He, H_2, and H_2O representing one-, two-, and three-center problems, respectively. For mapping parameters, L=1 is used for He and H_2, and L=0.5 for all nuclei of H_2O to refine more grid points around a heavy atom which has a steeper Coulomb potential. The computed integrals include normalization $n[\overline{\rho}]$, nucleus–electron interaction functional $E_{\rm ne}[\overline{\rho}]$, and exchange-only local density approximation (XLDA) functional $E_{\rm x}[\overline{\rho}]$,

$$n[\overline{\rho}] = \frac{1}{N_{\rm elec}}\int \overline{\rho}(\mathbf{x})d\tau, \tag{26}$$

$$E_{\rm ne}[\overline{\rho}] = \int \sum_\alpha \frac{Z_\alpha}{|\mathbf{x}_\alpha-\mathbf{x}|}\overline{\rho}(\mathbf{x})d\tau, \tag{27}$$

$$E_{\rm x}[\overline{\rho}] = -\frac{3}{4}\left(\frac{3}{\pi}\right)^{1/3}\int \overline{\rho}(\mathbf{x})^{4/3}d\tau, \tag{28}$$

where $N_{\rm elec}$ is the number of electrons, and $\mathbf{x}_\alpha$ and Z_α are the nuclear position and charge of the αth nucleus, respectively. Here, $\overline{\rho}$ is converged Gaussian-type orbital (GTO)-based density which consists of linear combination of GTOs obtained from LCAO calculations with the aug-cc-pVQZ basis set [72]. Note that exact values of $n[\overline{\rho}]$ and $E_{\rm ne}[\overline{\rho}]$ are computed by the analytical integration, while an exact value of $E_{\rm x}[\overline{\rho}]$ is computed by the multicenter numerical integration [14] and fully converged with large quadrature points. In Table 3, the error percentages on the normalization of the density are less than 0.68%, and decrease as the number of grid points increases. Also the error percentages on other energy functionals are almost the same as ones on the normalization for the same number of grid points. Note that these integration errors do not contaminate solutions of the eigenvalue problem because the Hamiltonian matrix in VFD is constructed without any integration.

Because eigenvectors in VFD computed by Eqs. (14) and

Table 3: Tests of VFD integrals for one-, two-, and three-center problems

Molecule	Grid ($N_r/l_{\max}$)	$n[\overline{\rho}]$	δ (%)	$E_{\rm ne}[\overline{\rho}]$	δ (%)	$E_{\rm x}[\overline{\rho}]$	δ (%)
He	120/20	1.006 337	0.63	−6.610 486	0.65	−0.858 062	0.62
	200/26	1.003 578	0.36	−6.591 954	0.36	−0.855 769	0.35
	300/32	1.002 310	0.23	−6.583 447	0.23	−0.854 706	0.23
	400/38	1.001 628	0.16	−6.578 890	0.16	−0.854 130	0.16
	Exact	1.000 000		−6.568 063		−0.852 750	
H_2	120/20	1.006 433	0.64	−3.588 689	0.63	−0.554 628	0.62
	200/26	1.003 620	0.36	−3.578 969	0.36	−0.553 154	0.35
	300/32	1.002 325	0.23	−3.574 453	0.23	−0.552 465	0.23
	Exact	1.000 000		−3.566 205		−0.551 199	
H_2O	120/20	1.006 816	0.68	−199.463 401	0.70	−8.099 123	0.65
	200/26	1.003 743	0.37	−198.845 443	0.38	−8.075 928	0.37
	300/32	1.002 376	0.24	−198.567 578	0.24	−8.065 431	0.24
	Exact	1.000 000		−198.083 473		−8.046 506	

(15) are always normalized to the unity by means of the VFD integration in Eq. (16),

$$\int \left|\psi^{(k)}(\mathbf{x})\right|^2 d\tau = \sum_i \left|c_i^{(k)}\right|^2 \nu_i = \sum_i \left|\tilde{c}_i^{(k)}\right|^2 = 1, \qquad (29)$$

the density computed by VFD becomes smaller than the true density by the amount of the normalization factor $n[\overline{\rho}]$. Even though this factor surely diminishes when the number of grid points becomes larger, it affects the exchange–correlation and Hartree potentials computed by the density and successively quality of DFT calculations. From this consideration, the density obtained by VFD can be scaled by the normalization factor computed from the GTO-based density in order to correctly compute the exchange–correlation and Hartree potentials,

$$\rho_{\rm norm} = \rho \times n[\overline{\rho}]. \qquad (30)$$

For energy functionals, we also use energy functionals with the normalization factor correction to reduce errors occurring at normalization,

$$E_{\rm norm}[\rho] = \frac{E[\rho_{\rm norm}]}{n[\overline{\rho}]}. \qquad (31)$$

This artificial normalization factor is introduced to compensate for inaccuracy of the simplest nodal quadrature in Eq. (16). It is possible to avoid this factor if the high-order scheme of integration is employed.

To examine how this normalization factor on the density affects DFT results, we compare XLDA energies of H_2 with and without the normalization factor correction in Table 4. The internuclear distance of H_2 is fixed at R=1.4 a.u. Table 4 includes the highest occupied molecular orbital (HOMO) and total energies, denoted as $\varepsilon_{\rm HOMO}$ and $E_{\rm total}$, respectively. Exact XLDA values for this diatomic molecule are obtained by the GPS method that accurately computes $\varepsilon_{\rm HOMO} = -0.331\,463$ a.u. and $E_{\rm total} = -1.043\,685$ a.u. with only 20 and 6 grid points for the ξ and η coordinates in the prolate spheroidal coordinates [73].

Table 4: XLDA energies (in a.u.) of H_2 at R=1.4 a.u.

Method	Grid ($N_r/l_{\max}$)	$\varepsilon_{\rm HOMO}$	$E_{\rm total}$
No NFC[a]	30/10	−0.360 2	−1.084 4
	50/15	−0.343 2	−1.060 6
	80/17	−0.339 1	−1.054 1
	120/20	−0.336 7	−1.050 6
	200/26	−0.334 4	−1.047 5
	300/32	−0.333 4	−1.046 1
NFC[b]	30/10	−0.330 5	−1.049 9
	50/15	−0.330 4	−1.045 7
	80/17	−0.331 1	−1.044 8
	120/20	−0.331 3	−1.044 4
	200/26	−0.331 4	−1.044 0
	300/32	−0.331 4	−1.043 9
Exact[c]		−0.331 5	−1.043 7

[a] VFD without the normalization factor correction
[b] VFD with the normalization factor correction
[c] Reference [73]

Note that the HOMO and total energies are getting close to exact values no matter whether the normalization factor correction is included or not. However, the results with the correction show faster convergence than ones without the correction and reach to sufficient accuracy ($|\delta| < 10^{-3}$ a.u.) with a relatively small number of grid points, $N_r \geq 120$ and $l_{\max} \geq 20$.

3.3. DFT calculations of many-electron polyatomic molecules

In the previous sections, we have shown that VFD provides an accurate and efficient Schrödinger equation solver for one-electron polyatomic molecules involving the multicenter Coulomb singularity, and developed VFD implementation for DFT including the Kohn–Sham and Poisson equation solvers and the normalization factor correction for accurate energy functional calculations. Now we explore the capability of the VFD method to perform DFT calculations of many-electron polyatomic molecules.

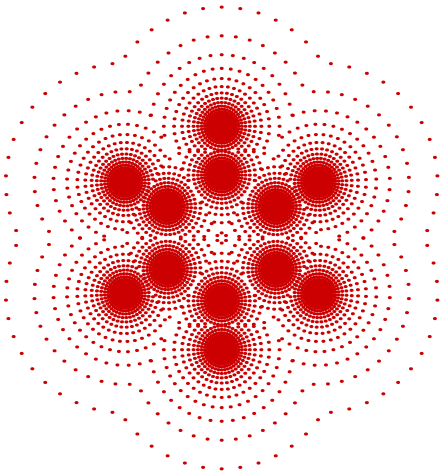

Figure 5: 2D sketch of multicenter molecular grids for benzene.

We present VFD–LDA results for nitrogen (N_2), water (H_2O), and benzene (C_6H_6) molecules. Figure 5 shows a 2D sketch of grid distribution for C_6H_6 assuring high adaptivity of multicenter molecular grids in VFD. Tables 5 to 7 include LDA orbital and total energies of N_2, H_2, and C_6H_6, respectively, computed by VFD and other methods. It is worthwhile to note that all calculations are performed with the realistic Coulomb potentials rather than the pseudopotentials, in order to compare accuracy regarding the Coulomb singularity. FD indicates the fourth-order finite difference method on uniform equal-spacing grids performed by Octopus [74]. The LCAO results is performed by Gamess [69] with aug-cc-pVQZ [72] for N_2 and H_2O; and 6-311++G(3df,3pd) [75] for C_6H_6. Note that these LCAO results are nearly converged to the complete basis set limit. The GPS results for diatomic N_2 [9] are also included for comparison. Molecular geometries used are (i) N_2: R(N–N)=2.072 a.u.; (ii) H_2O: R(O–H)=1.810 a.u. and $\angle$(H–O–H)=104.48°; (iii) C_6H_6: R(C–C)=2.640 a.u. and R(C–H)=2.048 a.u. Computational parameters for the VFD method are N_r=300, L=0.5, and $l_{\max}$=32 for all nuclei of N_2 and H_2O; and N_r=200, L=0.5, and $l_{\max}$=26 for all nuclei of C_6H_6. Total numbers of multicenter molecular grids are N_{grid}=592,532 for N_2, N_{grid}=1,115,453 for H_2O, and N_{grid}=1,943,646 for C_6H_6.

In Tables 5–7, one can see that the valence-electron orbital energies by VFD are comparable to ones by LCAO within less than 0.003 a.u., while core-electron orbital energies show discrepancies of 0.005–0.010 a.u. For the total energy, the VFD results successfully reproduce the LCAO results by less than 0.039 a.u. (0.01–0.04%) deviations. For N_2 in Table 5, the VFD results are in excellent agreement with both LCAO and GPS results, that the latter represents the most accurate results in this case. On the other hand, the conventional FD on uniform grids is not adequate to handle the Coulomb singularity, so affecting orbital and total energies significantly. For N_2, the valence-electron orbital energies by FD are deviated from the LCAO values by 0.004–0.049 a.u., the core-electron orbital energies

Table 5: LDA energies (in a.u.) of N_2 at R=2.072 a.u.

Orbital	FD[a]	LCAO[b]	VFD[c]	GPS[d]
$3\sigma_g$	−0.379	−0.383	−0.383	−0.383
$1\pi_u$	−0.411	−0.437	−0.438	−0.438
$2\sigma_u$	−0.543	−0.494	−0.494	−0.493
$2\sigma_g$	−1.048	−1.039	−1.038	−1.040
$1\sigma_u$	−14.958	−13.965	−13.971	−13.964
$1\sigma_g$	−14.959	−13.967	−13.972	−13.966
E_{total}	−114.100	−108.698	−108.737	

[a]Grid parameters: Δx=0.1 a.u. and $r_{\max}$=10 a.u.
[b]Basis set: aug-cc-pVQZ
[c]Grid parameters: N_r=300, L=0.5, and $l_{\max}$=32
[d]Reference [9]

Table 6: LDA energies (in a.u.) of H_2O with R(O–H)=1.810 a.u. and $\angle$(H–O–H)=104.48°.

Orbital	FD[a]	LCAO[b]	VFD[c]
$1b_1$	−0.281	−0.272	−0.273
$3a_1$	−0.341	−0.346	−0.346
$1b_2$	−0.487	−0.488	−0.488
$2a_1$	−0.898	−0.926	−0.927
$1a_1$	−17.935	−18.610	−18.620
E_{total}	−74.286	−75.912	−75.942

[a]Grid parameters: Δx=0.1 a.u. and $r_{\max}$=10 a.u.
[b]Basis set: aug-cc-pVQZ
[c]Grid parameters: N_r=300, L=0.5, and $l_{\max}$=32

Table 7: LDA energies (in a.u.) of C_6H_6 with R(C–C)=2.640 a.u. and R(C–H)=2.048 a.u.

Orbital	FD[a]	LCAO[b]	VFD[c]
$1e_{1g}$	−0.249	−0.240	−0.240
$3e_{2g}$	−0.310	−0.305	−0.303
$1a_{2u}$	−0.347	−0.341	−0.340
$3e_{1u}$	−0.382	−0.379	−0.377
$1b_{2u}$	−0.397	−0.407	−0.404
$2b_{1u}$	−0.415	−0.411	−0.410
$3a_{1g}$	−0.481	−0.478	−0.477
$2e_{2g}$	−0.531	−0.545	−0.543
$2e_{1u}$	−0.643	−0.676	−0.673
$2a_{1g}$	−0.741	−0.778	−0.775
$1b_{1u}$	−9.152	−9.790	−9.796
$1e_{2g}$	−8.858	−9.790	−9.797
$1e_{1u}$	−9.151	−9.791	−9.797
$1a_{1g}$	−9.152	−9.791	−9.797
E_{total}	−218.656	−230.177	−230.211

[a]Grid parameters: Δx=0.1 a.u. and $r_{\max}$=15 a.u.
[b]Basis set: 6-311++G(3df,3pd)
[c]Grid parameters: N_r=200, L=0.5, and $l_{\max}$=26

by 0.993 a.u., and the total energy by 5.402 a.u. (5.0%). The total energy for H_2O differs from the LCAO value by 1.626 a.u. (2.1%) and for C_6H_6 the deviation is 11.521 a.u. (5.0%). Moreover, FD with equal-spacing grids unavoidably uses a very large number of grid points to resolve the Coulomb singularity. For the N_2 case, the FD grid parameters are Δx=0.1 a.u. and $r_{\max}$=10 a.u., corresponding to the number of grid points $N_{\rm grid}$=4,187,857. In the meantime, the VFD grid parameters used for N_2 produce $N_{\rm grid}$=592,532 and the maximum radius becomes 150 a.u. Therefore, VFD utilizes less number of grid points covering much larger computational spaces than FD. Note that the proposed VFD method is the first-order scheme in the sense that it considers only nearest natural neighboring grids, while FD used here is the fourth-order scheme. Nonetheless, the numerical accuracy and efficiency of VFD are superior to ones of FD, mainly due to the benefit of the highly adaptive multicenter molecular grids.

4. Conclusion

We introduced the Voronoi-cell finite difference (VFD) method that realized a direct solution of the Schrödinger equation for polyatomic molecules on unstructured grids. Because of nodal adaptivity in the VFD method based on Voronoi cells and natural neighbors, we can utilize intuitive pictures for a molecular grid system that combines spherical atomic grids centered at nuclear positions, instead of regular and uniform grid distributions. With the VFD method, we solved the Schrödinger equation for one-electron systems within about 10^{-4} a.u. accuracy (0.1%) and showed that its accuracy was systematically improved by increasing the number of grid points. It was followed by extension to solve the Poisson and Kohn–Sham equations as well as nodal quadrature integration for implementation of DFT. We presented numerical LDA calculations for several polyatomic molecules. The VFD results were superior in accuracy to the ordinary FD results with uniform equal-spacing grids and comparable to the LCAO results with huge basis sets within about 0.04% deviation.

This VFD method opens a new path to numerically solve electronic structures of polyatomic molecules with the all-electron realistic Coulomb potential. As an accurate and efficient Kohn–Sham equation solver for polyatomic molecules, the VFD method has been advantageously suitable for time-dependent DFT calculations [50, 51] because it does not demand massive integration to construct the time-dependent Hamiltonian. In the present work, we have discussed only nearest natural neighbors as the first-order VFD method. It is also possible to include further neighbors to improve accuracy for the high-order VFD method in the future work.

Acknowledgments

The author thanks Dr. Shih-I Chu for initiating this work, and Dr. N. Sukumar, Dr. John E. Pask, Dr. Dmitry A. Telnov, Dr. Oriol Vendrell, and Dr. Young-Kyu Han for valuable discussions.

[1] F. Krausz, M. Ivanov, Attosecond physics, Rev. Mod. Phys. 81 (2009) 163–234.
[2] A. Szabo, N. S. Ostlund, Modern Quantum Chemistry, McGraw-Hill, New York, 1989.
[3] T. L. Beck, Real-space mesh techniques in density-funcitonal theory, Rev. Mod. Phys. 72 (2000) 1041–1080.
[4] K. C. Kulander (Ed.), Time-Dependent Methods for Quantum Dynamics, North-Holland, Amsterdam, 1991, reprinted from Comput. Phys. Commun., vol. 63 (1991) nos. 1-3.
[5] T. Kato, On the eigenfunctions of many-particle systems in quantum mechanics, Commun. Pure Appl. Math. 10 (1957) 151–177.
[6] S. I. Chu, Recent development of self-interaction-free time-dependent density-functional theory for nonperturbative treatment of atomic and molecular multiphoton processes in intense laser fields, J. Chem. Phys. 123 (2005) 062207.
[7] X. M. Tong, S. I. Chu, Theoretical study of multiple high-order harmonic generation by intense ultrashort pulsed laser fields: A new generalized pseudospectral time-dependent method, Chem. Phys. 217 (1997) 119–130.
[8] X. Chu, S. I. Chu, Self-interaction-free time-dependent density-functional theory for molecular processes in strong fields: High-order harmonic generation of H_2 in intense laser fields, Phys. Rev. A 63 (2001) 023411.
[9] X. Chu, S. I. Chu, Time-dependent density-functional theory for molecular processes in strong fields: Study of multiphoton processes and dynamical response of individual valence electrons of N_2 in intense laser fields, Phys. Rev. A 64 (2001) 063404.
[10] D. A. Telnov, S. I. Chu, *Ab initio* study of the orientation effects in multiphoton ionization and high-order harmonic generation from the ground and excited electronic states of H_2^+, Phys. Rev. A 76 (2007) 043412.
[11] J. F. Thompson, B. K. Soni, N. P. Weatherill, Handbook of Grid Generation, CRC Press, 1999.
[12] A. D. Becke, Basis-set-free density-functional quantum-chemistry, Int. J. Quant. Chem. Quant. Chem. Symp. 23 (1989) 599–609.
[13] R. M. Dickson, A. D. Becke, Basis-set-free local density-functional calculations of geometries of polyatomic molecules, J. Chem. Phys. 99 (1993) 3898–3905.
[14] A. D. Becke, A multicenter numerical integration scheme for polyatomic molecules, J. Chem. Phys. 88 (1988) 2547–2553.
[15] A. D. Becke, R. M. Dickson, Numerical solution of Schrödinger's equation in polyatomic molecules, J. Chem. Phys. 92 (1990) 3610–3612.
[16] G. Voronoï, Nouvelles applications des paramètres continus à la théorie des formes quadratiques. deuxième mémoire: Recherches sur les parallélloèdres primitifs, J. Reine Angew. Math. 134 (1908) 198–287.
[17] F. Aurenhammer, Voronoi diagrams – a survey of a fundamental geometric data structure, ACM Comput. Surv. 23 (1991) 345–405.
[18] A. Okabe, B. Boots, K. Sugihara, S. N. Chiu, Spatial Tessellations: Concepts and Applications of Voronoi Diagrams, 2nd Edition, John Wiley & Sons, Chichester, 2000.
[19] J. Braun, M. Sambridge, A numerical method for solving partial differential equations on highly irregular evolving grids, Nature 376 (1995) 655–660.
[20] N. Sukumar, B. Moran, A. Y. Semenov, V. V. Belikov, Natural neighbour Galerkin methods, Int. J. Numer. Meth. Engng 50 (2001) 1–27.
[21] E. Cueto, N. Sukumar, B. Calvo, M. A. Martínez, J. Cegoñino, M. Doblaré, Overview and recent advances in natural neighbour Galerkin methods, Arch. Comput. Meth. Engng. 10 (2003) 307–384.
[22] I. D. Mishev, Finite volume methods on Voronoi meshes, Numer. Methods Partial Differential Equations 14 (1998) 193–212.
[23] Q. Du, M. D. Gunzburger, L. Ju, Voronoi-based finite volume methods, optimal Voronoi meshes, and PDEs on the sphere, Comput. Methods Appl. Mech. Engrg. 192 (2003) 3933–3957.
[24] N. A. Gatsonis, A. Spirkin, A three-dimensional electrostatic particle-in-cell methodology on unstructured Delaunay–Voronoi grids, J. Comput. Phys. 228 (2009) 3742–3761.
[25] N. Sukumar, Voronoi cell finite difference method for the diffusion operator on arbitrary unstructured grids, Int. J. Numer. Meth. Engng 57 (2003) 1–34.
[26] N. Sukumar, J. E. Bolander, Numerical computation of discrete differential operators on non-uniform grids, CMES Comput. Model. Eng. Sci. 4 (2003) 691–705.
[27] N. Sukumar, R. W. Wright, Overview and construction of meshfree basis

functions: From moving least squares to entropy approximants, Int. J. Numer. Meth. Engng 70 (2007) 181–205.
[28] M. Griebel, M. A. Schweitzer (Eds.), Meshfree Methods for Partial Differential Equations, Vol. 26 of Lecture notes in computational science and engineering, Springer, Berlin, 2003.
[29] G. de Fabritiis, S. Succi, P. V. Coveney, Electronic structure calculations using self-adaptive multiscale Voronoi basis functions, J. Stat. Phys. 107 (2002) 159–171.
[30] J. Ackermann, B. Erdmann, R. Roitzsch, A self-adaptive multilevel finite element method for the stationary Schrödinger equation in three space dimensions, J. Chem. Phys. 101 (1994) 7643–7650.
[31] J. E. Pask, B. M. Klein, C. Y. Fong, P. A. Sterne, Real-space local polynomial basis for solid-state electronic-structure calculations: A finite-element approach, Phys. Rev. B 59 (1999) 12532–12358.
[32] S. Tonzani, C. H. Greene, Low-energy electron scattering from DNA and RNA bases: Shape resonances and radiation damage, J. Chem. Phys. 124 (2006) 054312.
[33] L. Lehtovaara, V. Havu, M. Puska, All-electron density functional theory and time-dependent density functional theory with high-order finite elements, J. Chem. Phys. 131 (2009) 054103.
[34] P. F. Batcho, Computational method for general multicenter electronic structure calculations, Phys. Rev. E 61 (2000) 7169–7183.
[35] F. Gygi, Electronic-structure calculations in adaptive coordinates, Phys. Rev. B 48 (1993) 11692–11700.
[36] N. A. Modine, G. Zumbach, E. Kaxiras, Adaptive-coordinate real-space electronic-structure calculations for atoms, molecules, and solids, Phys. Rev. B 55 (1997) 10289–10301.
[37] M. Heiskanen, T. Torsti, M. J. Puska, R. M. Nieminen, Multigrid method for electronic structure calculations, Phys. Rev. B 63 (2001) 245106.
[38] T. Torsti, M. Heiskanen, M. J. Puska, R. M. Nieminen, MIKA: Multigrid-based program package for electronic structure calculations, Int. J. Quant. Chem. 91 (2003) 171–176.
[39] J. Wang, T. L. Beck, Efficient real-space solution of the Kohn–Sham equations with multiscale techniques, J. Chem. Phys. 112 (2000) 9223–9228.
[40] T. A. Arias, Multiresolution analysis of electronic structure: semicardinal and wavelet bases, Rev. Mod. Phys. 71 (1999) 267–311.
[41] R. J. Harrison, G. I. Fann, T. Yanai, Z. Gan, G. Beylkin, Multiresolution quantum chemistry: Basic theory and initial applications, J. Chem. Phys. 121 (2004) 11587–11598.
[42] T. Yanai, G. I. Fann, Z. Gan, R. J. Harrison, G. Beylkin, Multiresolution quantum chemistry in multiwavelet bases: Hartree–Fock exchange, J. Chem. Phys. 121 (2004) 6680–6688.
[43] D. Toffoli, M. Stener, G. Fronzoni, P. Decleva, Convergence of the multicenter B-spline DFT approach for the continuum, Chem. Phys. 276 (2002) 25–43.
[44] T. N. Rescigno, D. A. Horner, F. L. Yip, C. W. McCurdy, Hybrid approach to molecular continuum processes combining Gaussian basis functions and the discrete variable representation, Phys. Rev. A 72 (2005) 052709.
[45] J. R. Chelikowsky, N. Troullier, Y. Saad, Finite-difference-pseudopotential method: Electronic structure calculations without a basis, Phys. Rev. Lett. 72 (1994) 1240–1243.
[46] J. R. Chelikowsky, N. Troullier, K. Wu, Y. Saad, Higher-order finite-difference pseudopotential method: An application to diatomic molecules, Phys. Rev. B 50 (1994) 11355–11364.
[47] D. J. Singh, Planewaves, Pseudopotentials, and the LAPW Method, Kluwer Academic, Boston, 1994.
[48] R. Sibson, A vector identity for the Dirichlet tessellation, Math. Proc. Cambridge Philos. Soc. 87 (1980) 151–155.
[49] C. B. Barber, D. P. Dobkin, H. Huhdanpaa, The quickhull algorithm for convex hulls, ACM Trans. Math. Software 22 (1996) 469–483.
URL `http://www.qhull.org/`
[50] S.-K. Son, S. I. Chu, Multielectron effects on the orientation dependence and photoelectron angular distribution of multiphoton ionization of CO_2 in strong laser fields, Phys. Rev. A 80 (2009) 011403(R).
[51] S.-K. Son, S. I. Chu, Theoretical study of orientation-dependent multiphoton ionization of polyatomic molecules in intense ultrashort laser fields: A new time-dependent Voronoi-cell finite difference method, Chem. Phys. 366 (2009) 91–102.
[52] G. B. Arfken, H. J. Weber, Mathematical Methods for Physicists, 5th Edition, Harcourt/Academic Press, San Diego, 2001.
[53] D. González, E. Cueto, M. A. Martínez, M. Doblaré, Numerical integration in natural neighbour Galerkin methods, Int. J. Numer. Meth. Engng 60 (2004) 2077–2104.
[54] P. S. Jensen, Finite difference techniques for variable grids, Comput. & Structures 2 (1972) 17–29.
[55] T. Liszka, J. Orkisz, The finite difference method at arbitrary irregular grids and its application in applied mechanics, Comput. & Structures 11 (1980) 83–95.
[56] M. Vinokur, An analysis of finite-difference and finite-volume formulations of conservation laws, J. Comput. Phys. 81 (1989) 1–52.
[57] J. M. Hyman, R. J. Knapp, J. C. Scovel, High order finite volume approximations of differential operators on nonuniform grids, Physica D 60 (1992) 112–138.
[58] R. J. LeVeque, Finite volume methods for hyperbolic problems, Cambridge University Press, New York, 2002.
[59] P. Hohenberg, W. Kohn, Inhomogeneous electron gas, Phys. Rev. 136 (1964) B864–B871.
[60] R. G. Parr, W. Yang, Density-Functional Theory of Atoms and Molecules, Vol. 16 of International series of monographs on chemistry, Oxford University Press, New York, 1989.
[61] S. H. Vosko, L. Wilk, M. Nusair, Accurate spin-dependent electron liquid correlation energies for local spin density calculations: a critical analysis, Can. J. Phys. 58 (1980) 1200–1211.
[62] B. G. Johnson, P. M. W. Gill, J. A. Pople, The performance of a family of density functional methods, J. Chem. Phys. 98 (1993) 5612–5626.
[63] W. Kohn, L. J. Sham, Self-consistent equations including exchange and correlation effects, Phys. Rev. 140 (1965) A1133–A1138.
[64] C. Canuto, M. Y. Hussaini, A. Quarteroni, T. A. Zang, Spectral Methods in Fluid Dynamics, Springer-Verlag, New York, 1988.
[65] V. I. Lebedev, Quadratures on a sphere, Comput. Math. Math. Phys. 16 (1976) 10–24.
[66] M. M. Madsen, J. M. Peek, Eigenparameters for the lowest twenty electronic states of the hydrogen molecule ion, At. Data 2 (1971) 171–204.
[67] R. B. Lehoucq, D. C. Sorensen, C. Yang, ARPACK Users' Guide: Solution of Large-Scale Eigenvalue Problems with Implicitly Restarted Arnoldi Methods, SIAM, Philadelphia, 1998.
URL `http://www.caam.rice.edu/software/ARPACK/`
[68] O. Schenk, K. Gärtner, On fast factorization pivoting methods for symmetric indefinite systems, Elec. Trans. Numer. Anal. 23 (2006) 158–179.
URL `http://www.pardiso-project.org/`
[69] M. W. Schmidt, K. K. Baldridge, J. A. Boatz, S. T. Elbert, M. S. Gordon, J. H. Jensen, S. Koseki, N. Matsunaga, K. A. Nguyen, S. Su, T. L. Windus, M. Dupuis, J. A. Montgomery, Jr., General atomic and molecular electronic structure system, J. Comput. Chem. 14 (1993) 1347–1363.
URL `http://www.msg.chem.iastate.edu/gamess/`
[70] K. A. Peterson, D. E. Woon, J. Thom H. Dunning, Benchmark calculations with correlated molecular wave functions. IV. The classical barrier height of the $H+H_2 \rightarrow H_2+H$ reaction, J. Chem. Phys. 100 (1994) 7410–7415.
[71] J. C. L. Vieyra, A. V. Turbiner, H_3^{2+} molecular ion in a strong magnetic field: Triangular configuration, Phys. Rev. A 66 (2002) 023409.
[72] T. H. Dunning, Jr., Gaussian basis sets for use in correlated molecular calculations. I. The atoms boron through neon and hydrogen, J. Chem. Phys. 90 (1989) 1007–1023.
[73] D. A. Telnov, private communication.
[74] A. Castro, H. Appel, M. Oliveira, C. A. Rozzi, X. Andrade, F. Lorenzen, M. A. L. Marques, E. K. U. Gross, A. Rubio, `octopus`: a tool for the application of time-dependent density functional theory, Phys. Status Solidi B 243 (2006) 2465–2488.
[75] R. Krishnan, J. S. Binkley, R. Seeger, J. A. Pople, Self-consistent molecular orbital methods. XX. A basis set for correlated wave functions, J. Chem. Phys. 72 (1980) 650–654.